Journal of
Mechanics of
Materials and Structures

HIERARCHICAL MULTISCALE MODELING OF THE EFFECT OF CARBON NANOTUBE DAMAGE ON THE ELASTIC PROPERTIES OF POLYMER NANOCOMPOSITES

G. Domínguez-Rodríguez, A. K. Chaurasia, G. D. Seidel, A. Tapia and F. Avilés

Volume 12, No. 3 May 2017

msp

JOURNAL OF MECHANICS OF MATERIALS AND STRUCTURES
Vol. 12, No. 3, 2017
dx.doi.org/10.2140/jomms.2017.12.263

HIERARCHICAL MULTISCALE MODELING OF THE EFFECT OF CARBON NANOTUBE DAMAGE ON THE ELASTIC PROPERTIES OF POLYMER NANOCOMPOSITES

G. DOMÍNGUEZ-RODRÍGUEZ, A. K. CHAURASIA, G. D. SEIDEL, A. TAPIA AND F. AVILÉS

The influence of various levels of carbon nanotube (CNT) structural damage on the transversely isotropic elastic properties of CNTs and CNT/polymer composites is investigated through a hierarchical multiscale modeling strategy. Assessment of the effect of structural damage on the CNTs is first conducted by removing C-C bonds and using atomistic finite element analysis. The composite cylinder method is then used to model composites whose effective properties are obtained from the Mori–Tanaka method. The axial, radial, transverse shear and in-plane shear moduli of CNTs decrease $\sim 70\%$ for 10% damage. This decrease is more pronounced for CNTs with small radii, and when the broken bonds coalesce. The transverse Poisson's ratio of CNTs increases about six times for 10% damage. When these defective CNTs are used in polymer composites, the axial elastic modulus of the composite reduces by $\sim$80% while the transverse Poisson's ratio increases about three times.

1. Introduction

The engineering applications of carbon nanotube (CNT) reinforced polymers are numerous [De Volder et al. 2013]. It is well-known that adding small quantities of CNTs can enhance the mechanical and electrical properties of their host polymer, creating multifunctional materials [Gates et al. 2005; Fukushima et al. 2006; Spitalsky et al. 2010]. The transportation and aerospace industries are examples of potential users, where low density, high strength, and multifunctionality are important for service and design.

Different forms of structural damage have been reported for CNTs and other sp^2/sp^3 carbon-based nanostructures. Structural defects are commonly generated during the CNT synthesis, or by postsynthesis treatments such as electron/ion irradiation or chemical methods [Balog et al. 2010; Banhart 1999; Banhart et al. 2011; Kim et al. 2009; Krasheninnikov and Banhart 2007; Lucchese et al. 2010]. A common kind of topological CNT defect is the one frequently called "Stone–Wales" defect (although it has been suggested that a "Thrower" defect is a more proper name [Monthioux and Charlier 2014]), where two carbon atoms rotate to transform four hexagons into two heptagons and two pentagons [Araujo et al. 2012; Banhart et al. 2011]; see Figure 1, left. A second kind of defect are vacancies, i.e., places where an atom is missing; vacancies can be single (Figure 1, center) or formed by more than one missing atom (Figure 1, right).

Defects are associated with a degradation of mechanical properties of CNTs [Shet et al. 2005], with vacancies being more influential than Thrower-type defects [Sammalkorpi et al. 2004; Zandiatashbar et al. 2014]. According to Talukdar and Mitra [2010] and Sharma et al. [2012], a Thrower defect can reduce the axial elastic modulus of a singlewall CNT (SWCNT) up to 6%. In contrast, molecular dynamics

Keywords: Mori–Tanaka, composite cylinder method, SWCNT, polymer, elastic properties, multiscale, FEA.

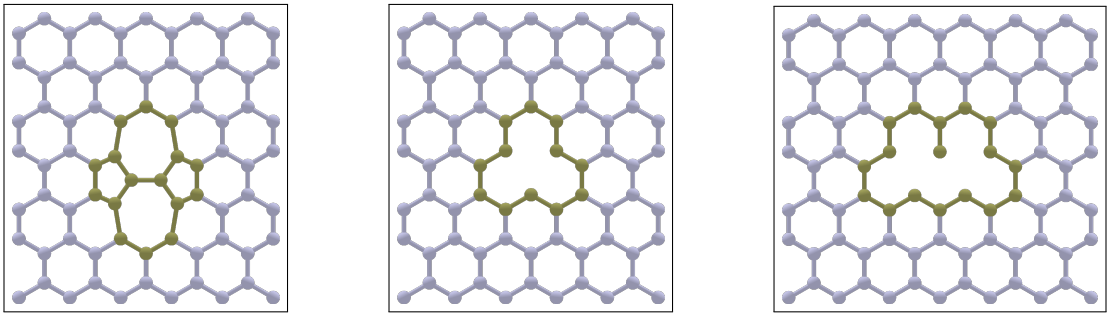

Figure 1. Different kinds of topological defects present in carbon nanostructures: left, Thrower defect; center, single vacancy; right, double vacancy.

simulations predict a reduction of about 10% in the elastic modulus for a concentration of vacancies of 2.5% [Fefey et al. 2011] and about 40% for a concentration of vacancies of 8%[Yuan and Liew 2009]. Mielke et al. [2004] and Tserpes et al. [2007] showed that Thrower defects and vacancies are important causes of tensile fracture.

Structural defects such as vacancies are able to rearrange their topology to minimize their formation energy [Yuan and Liew 2009; Berber and Oshiyama 2006]. During this rearrangement, new bonds are formed and others broken. Some defects, such as Thrower-type, do not reduce the number of bonds, while others, such as vacancies, reduce the number of bonds by two or three bonds, with a corresponding energy reconfiguration [Mielke et al. 2004; Tserpes and Papanikos 2007]. Modeling the dynamic rearrangement process after bond elimination is a complex task which demands dedicated *ab initio* computations [Gallo et al. 2007; Prasomsri et al. 2010; Ahangari et al. 2013] that are very limited in size. Traditional density functional theory computations are in the range of a few hundreds of atoms and can only reach thousands for clusters with hundreds of cores [Kohn 1995; Fonseca Guerra et al. 1998; Hine et al. 2009]. An alternative approach to tackle this problem is by finite element analysis (FEA). Although FEA does not account for quantum effects needed to predict the rearrangement of structural defects after relaxation, within the Newtonian mechanics framework FEA is a versatile and accurate tool to efficiently predict elastic properties of nanostructures [Giannopoulos et al. 2013; Haghbin and Khalili 2014; Domínguez-Rodríguez et al. 2014]. To date, bridging scales to predict elastic properties of polymer composites seems to be plausible only by using classical mechanics modeling tools. Continuous homogenization models have been previously conducted for macroscopic lattices in order to simplify the prediction of the mechanical properties of beam structures [Noor et al. 1978; Sun et al. 1981; Noor 1988; Dow and Huyer 1989; Sun and Liebbe 1990; Usik 1994]; more recently they have also been applied to nanostructures such as graphene sheets and CNTs [Odegard et al. 2002; Blanc et al. 2002; Caillerie et al. 2006]. In the present work, a hierarchical multiscale modeling approach is undertaken, wherein FEA is used at the smallest scale to predict the (transversely isotropic) elastic properties of SWCNTs. In order to damage the CNTs, carbon-carbon (C-C) bonds are sequentially eliminated. Two approaches for bond elimination are used. In the first one, bonds are randomly broken without consideration of the previous damage state; in the second one, the sequential bond breaking process is conducted only at adjacent bonds, simulating clustering damage. These properties are then used as an input to compute the influence of such CNT structural defects on the elastic properties of SWCNT/polymer composites, using classical

micromechanics theories. The composite cylinder method [Hashin and Rosen 1964] is then used to model the elastic properties of a CNT/polymer composite using the local orientation scale and including an interphase, whereas the Mori–Tanaka (MT) method [1973] is used to predict the elastic properties of composites including CNTs with multiple orientations, chiralities, and damage severity.

2. Methodology

2.1. ***Elastic properties of a transversely isotropic CNT.*** CNTs can be treated as transverse isotropic materials, which means that five independent elastic properties are needed to construct their stiffness tensor. The five independent elastic properties chosen for investigation in the current work are the axial elastic modulus (E_{11}), the in-plane bulk modulus (K_{23}), the transverse Poisson's ratio (ν_{12}), the transverse shear modulus (μ_{12}) and the in-plane shear modulus (μ_{23}). Here, 1, 2 and 3 represent the axial, radial and angular directions of the local material coordinates of the CNT, respectively, whereas x, y, and z are the orthogonal axes of the global Cartesian coordinates as shown in Figure 2. Here, r is the radial position and θ is the angle between the axes x and 2. The CNT stiffness tensor is defined by [Qu and Cherkaoui 2006]

$$C_{ij} = \begin{pmatrix} C_{11} & C_{12} & C_{12} & 0 & 0 & 0 \\ C_{12} & C_{22} & C_{23} & 0 & 0 & 0 \\ C_{12} & C_{23} & C_{22} & 0 & 0 & 0 \\ 0 & 0 & 0 & \mu_{23} & 0 & 0 \\ 0 & 0 & 0 & 0 & \mu_{12} & 0 \\ 0 & 0 & 0 & 0 & 0 & \mu_{12} \end{pmatrix}, \tag{1}$$

where $C_{11} = E_{11} + 4\nu_{12}^2 K_{23}$ and $C_{12} = 2\nu_{12} K_{23}$ and $C_{22} = K_{23} + \mu_{23}$ and $C_{23} = K_{23} - \mu_{23}$.

The definition of the transverse Poisson's ratio for defective CNTs may be ambiguous, since structural defects produce localized perturbations in the displacement field that can differ greatly from the free transverse contraction. Therefore, the axial component of the stiffness tensor (C_{11}) was obtained from

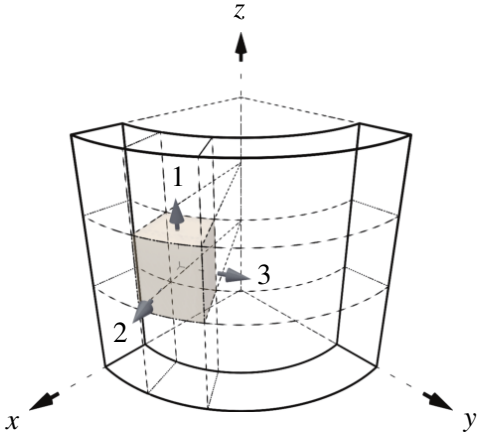

Figure 2. Material coordinates used in this work.

an energy balance and is used here to predict the transverse Poisson's ratio as

$$\nu_{12} = \sqrt{\frac{C_{11} - E_{11}}{4K_{23}}}. \tag{2}$$

The radial elastic modulus (E_{22}) was obtained from the axial elastic modulus (E_{11}), the transverse Poisson's ratio (ν_{12}), the in-plane bulk (K_{23}), and shear moduli (μ_{23}) as

$$E_{22} = \frac{4K_{23}\mu_{23}}{K_{23} + \mu_{23} + 4\nu_{12}^2 K_{23}\mu_{23}/E_{11}}. \tag{3}$$

2.2. ***Finite element analysis of defective CNTs.*** The atomistic FEA proposed by Li and Chou [2003b] was used here to predict the elastic properties of CNTs. In this method, the atoms are considered as nodes and the C-C bonds are modeled as solid beams with a circular cross section, whose elastic modulus (E_{beam}) and shear modulus (G_{beam}) are obtained from an equivalence between the structural deformation energies and the molecular mechanics potentials associated with tension, bending, and torsion of the atomic bonds. The selection of the beam's cross-section does not affect the calculations as long as the area and moment of inertia are preserved [Li and Chou 2003b]. Each type of bond deformation is associated with a bond force constant, representing tension (k_T), bending (k_B), and torsion (k_τ) [Li and Chou 2003b]. The elastic and geometric properties of the beams that model the C-C bonds are defined as [Li and Chou 2003b; Sakhaee-Pour 2009]

$$d_{\text{beam}} = 4\sqrt{\frac{k_B}{k_T}}, \quad E_{\text{beam}} = \frac{k_T^2 L_{\text{beam}}}{4\pi k_B}, \quad G_{\text{beam}} = \frac{k_T^2 k_\tau L_{\text{beam}}}{8\pi k_B^2}, \tag{4}$$

where d_{beam} is the beam's diameter, E_{beam} is the beam's elastic modulus, G_{beam} its shear modulus, and L_{beam} is the C-C bond length. Following the recommendations of Li and Chou [2003b], a C-C bond length of $L_{\text{beam}} = 0.142\,\text{nm}$ and bond force constants of $k_T = 6.52 \cdot 10^{-7}\,\text{N}\cdot\text{nm}^{-1}$ and $k_B = 8.76 \cdot 10^{-10}\,\text{N}\cdot\text{nm}^{-1}\cdot\text{rad}^2$ and $k_\tau = 2.78 \cdot 10^{-10}\,\text{N}\cdot\text{nm}^{-1}\cdot\text{rad}^2$ were employed, as reported by Cornell et al. [1995] and Jorgensen and Severance [1990] for benzene.

The numerical solution was conducted through the commercial code ANSYS 13.0, using the "BEAM4" element which allows bending, torsion, axial compression, and tension.

Following the method of Li and Chou [2003b], nonbonded interactions such as van der Waals forces are neglected, given their significantly lower contribution when compared to covalent interactions, especially for SWCNTs [Li and Chou 2003a; Kalamkarov et al. 2006]. However, it is important to notice that van der Waals forces might be relevant for interactions between layers for the case of multiwall CNTs [Li and Chou 2003a].

Armchair SWCNTs of different chiralities were considered ranging from (3,3) (with a radius of $R \approx 0.2\,\text{nm}$) to (10,10) ($R \approx 0.7\,\text{nm}$), containing a total number of 200 unit cells of height $H = 2.46\,\text{Å}$ (see Figure 3) for a total CNT length of $L = 49.2\,\text{nm}$. This length, albeit short, keeps the problem computationally tractable and was proven to yield mechanical properties which are independent of the CNT length in a previous analysis [Domínguez-Rodríguez et al. 2014]. An equivalent wall thickness of $t = 3.4\,\text{Å}$ was considered for homogenization purposes, which is equivalent to the interlayer distance between graphene sheets [Ferrari and Basko 2013; Gao et al. 2008; Ni et al. 2007; Blake et al. 2007;

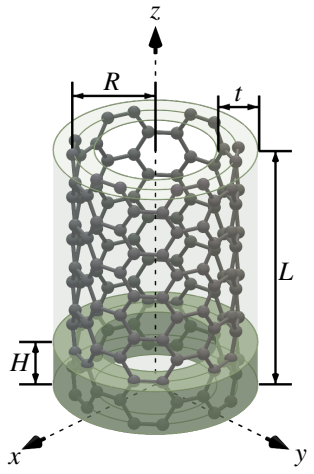

Figure 3. Geometric parameters of a representative SWCNT.

Burnett et al. 2012; Novoselov et al. 2005; Obraztsova et al. 2008]; see Figure 3. The selection of other wall thicknesses may significantly change the elastic properties of CNTs when homogenized as a hollow cylinder [Demczyk et al. 2002; Zhang et al. 2002; Srivastava et al. 2003; Natsuki et al. 2004; Tserpes and Papanikos 2005]. However, if homogenized as an effective solid cylinder, the values of the effective CNT properties would change marginally with the wall thickness.

2.2.1. *Loading cases.* The five loading cases depicted in Figure 4 were chosen in order to calculate the five independent elastic properties of the SWCNT considered as a transversely isotropic material. The total strain energy was computed for each loading case and the corresponding elastic property was obtained through an energy balance, to be further discussed. Specific boundary conditions for each loading case were imposed by applying linear equations representing the constraints on the displacement field as functions of the radial (u_r), angular (u_θ), and axial (u_z) displacement fields. The applied strain (ϵ_r, $\epsilon_{r\theta}$, ϵ_{zr} or ϵ_z) was set to 0.02, although the resulting elastic properties are independent of this input value.

In order to obtain the axial elastic modulus of the CNT (E_{11}^{CNT}), an axial (z) strain ($\epsilon_z = 0.02$) was applied through a displacement field $u_z = \epsilon_z L$ at the atoms located at the top edge of the CNT ($z = L$), whereas all degrees of freedom were restricted at the bottom edge ($z = 0$) of the SWCNT ($u_r|_{z=0} = u_z|_{z=0} = u_\theta|_{z=0} = 0$); see Figure 4a. The rest of the atoms were allowed to move freely in this loading case.

For simulation of the radial expansion to determine K_{23}^{CNT}, the top and bottom atoms were restricted to prevent contraction or expansion along the axial direction ($u_z|_{z=0} = u_z|_{z=L} = 0$), and a radial displacement $u_r = r\epsilon_r$ was applied to all of the nodes; see Figure 4b.

In order to obtain C_{11}^{CNT}, an axial strain (ϵ_z) was applied through a displacement $u_z = \epsilon_z L$ at the top edge atoms ($z = L$), whereas u_z was set to zero at the bottom edge atoms ($z = 0$). Displacements u_r and u_θ were restricted for all atoms in this loading case, as shown in Figure 4c.

For defective CNTs, the conventional definition of the transverse Poisson's ratio (ν_{12}^{CNT}) extracted directly from the transverse contraction of the axial strain loading case (Figure 4a) may be ambiguous, given the excessive localized transverse deformation in the vicinity of the defect. Thus, ν_{12}^{CNT} was calculated here from a combination of E_{11}^{CNT}, C_{11}^{CNT} and K_{23}^{CNT} as stated in (2).

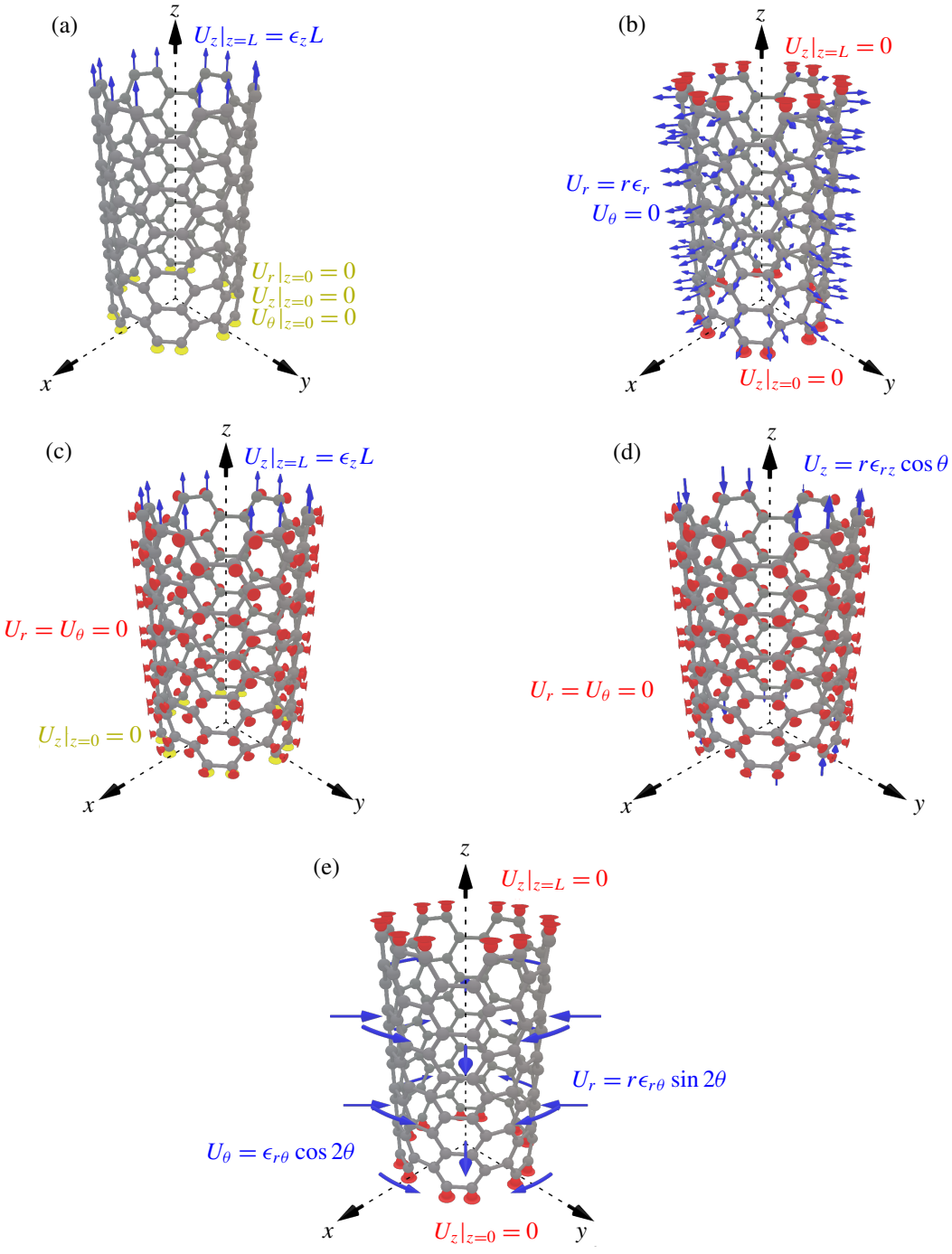

Figure 4. Loading cases used in FEA to determine the five independent elastic constants of the SWCNT: a, axial strain (E_{11}^{CNT}); b, radial expansion (K_{23}^{CNT}); c, axial strain with radial restriction (C_{11}^{CNT}, ν_{12}^{CNT}); d, transverse shear strain (μ_{12}^{CNT}); and e, in-plane shear strain (μ_{23}^{CNT}).

The transverse shear modulus (μ_{12}^{CNT}) was determined by applying a transverse shear strain (ϵ_{rz}) modeled as a nonuniform displacement field $u_z = r\epsilon_{rz}\cos(\theta)$ for all atoms, while u_r and u_θ were restricted to zero for all nodes to prevent contraction and rotation of the CNT; see Figure 4d.

Finally, to compute the in-plane shear modulus (μ_{23}^{CNT}), nonuniform radial and tangential displacement fields of magnitude $u_r = r\epsilon_{r\theta}\sin(2\theta)$ and $u_\theta = \epsilon_{r\theta}\cos(2\theta)$ were applied, whereas the top and bottom atoms were restricted to prevent contraction or expansion along the axial direction ($u_z|_{z=0} = u_z|_{z=L} = 0$); see Figure 4e. This loading case simulates the application of an in-plane (xy) shear strain.

2.2.2. *Energy balance.* In order to obtain the elastic properties of the investigated SWCNTs, the strain energy of the CNT's structural model was set equal to the strain energy of a solid cylinder under the same boundary conditions [Hashin and Rosen 1964], i.e.,

$$\frac{1}{V_C}\sum_{n=1}^{N} E_n^{(\mathrm{B})} = \frac{1}{2V_C}\int_0^L\int_0^{2\pi}\int_0^{R+t/2} (\boldsymbol{\sigma} : \boldsymbol{\epsilon}) r \, \partial r \, \partial\theta \, \partial z, \tag{5a}$$

where $E_n^{(B)}$ is the total strain energy of the n-th C-C beam, N is the number of beams (or C-C bonds), V_C is the volume of the CNT considered as a solid cylinder (to avoid interdependency among the five elastic properties) and : represents the Frobenius inner product defined for dyadics [Meyer 2000].

Since the strains are not functions of z and $V_C = \pi\left(R + \frac{1}{2}t\right)^2 L$, (5a) becomes

$$\frac{1}{L}\sum_{n=1}^{N} E_n^{(\mathrm{B})} = \frac{1}{2}\int_0^{2\pi}\int_0^{R+t/2} (\boldsymbol{\sigma} : \boldsymbol{\epsilon}) r \, \partial r \, \partial\theta. \tag{5b}$$

The evaluation of (5b) provides three linear equations for E_{11}^{CNT} and C_{11}^{CNT} and μ_{12}^{CNT} and a set of two linear algebraic equations whose solution yields μ_{23}^{CNT} and K_{23}^{CNT}. Because of the CNT central hollow area, (5b) shows a dependency of R and t on the CNT elastic properties. All five independent elastic properties are used to construct the stiffness tensor listed in (1).

2.2.3. *Damage generation.* The approach used here to simulate structural defects was to sequentially eliminate C-C bonds. Two configurations were investigated depending on the sequence of bond elimination followed, viz. randomly generated damage (Figure 5, top) or clustered damage (Figure 5, bottom). Since each carbon atom has three bonds, breakage of the three bonds may be considered as a vacancy in terms of missing bonds. In the random evolution scenario, the bonds are removed by generating random numbers following a uniform distribution of probability from 0 to 1. The bond is deemed broken if the randomly generated number is lower than the fraction of broken bonds to be simulated (broken bonds/total number of bonds). Due to the random nature of the process, the computations were repeated numerous times and the results averaged, reporting the average value of the computed elastic property. A dedicated convergence analysis showed that 40 repetitions yielded differences less than 0.2% for all elastic properties and damage states with respect to results with 80 of repetitions; thus 40 iterations was deemed convergent.

CNT damage was also modeled following a clustering pattern. In this approach, the first broken bond was randomly generated, and the following broken bonds were restricted to be chosen from the neighbors of the already broken bonds, generating clustered damage (Figure 5, bottom). The clustering pattern produces coalescence of CNT damage and is expected to severely affect the SWCNT properties;

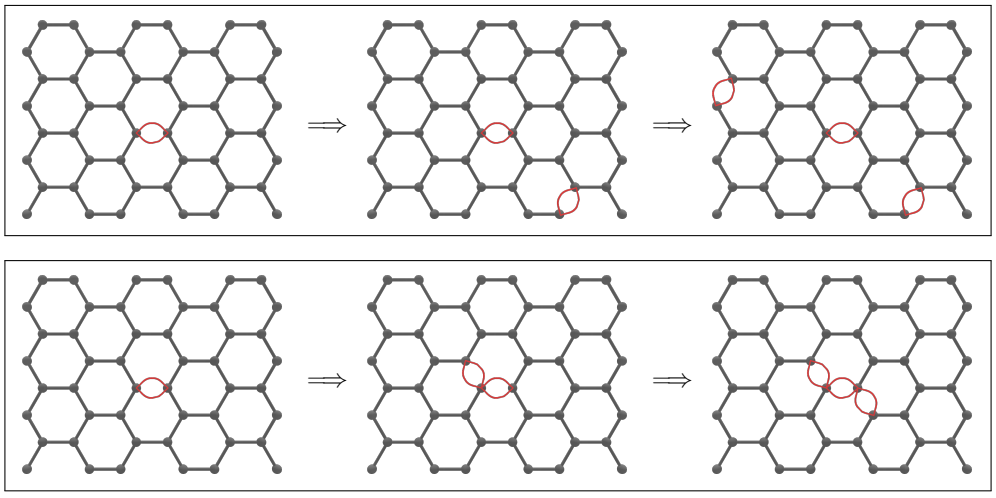

Figure 5. Schematic representation of the two cases of damage evolution investigated: top, random; bottom, clustered.

see, e.g., [Sammalkorpi et al. 2004]. Therefore, even when quantum bond reconstruction is not addressed in our classical mechanics approach, the clustered damage is expected to represent an upper bound for the same fraction of broken bonds.

2.3. *Prediction of the elastic properties of axially oriented CNT/polymer composites.*

2.3.1. *Composite cylinder method.* The composite cylinder method (CCM), initially proposed by Hashin and Rosen [1964], was used to predict the elastic properties of composite materials represented by concentric cylindrical layers. In the CCM, each layer (numbered from 1 to N) represents a phase with its own elastic properties, schematically represented as C^i for illustration purposes in Figure 6. The CCM method was employed here to predict the elastic properties of perfectly oriented polymer composites containing CNTs, including an interphase, whose stiffness tensor varies as a piecewise constant from that of the CNT (C^{CNT}) to the one of the matrix (C^m) [Hernández-Pérez and Avilés 2010]; see Figure 6. The stiffness tensor of the CNT was obtained from the energy balance between the strain energies of the CNT structure and the solid cylinder; see (5). The interface between two adjacent interphases is considered perfect, i.e., the stress tensor transfers from one layer to the other without loss. The number of interphase layers was set to 5. While a higher number of interphase layers may increase precision, it also increases the computational burden and more than 5 interphase layers was not deemed necessary in this work, provided a proper convergence analysis. The center (first phase) represents the CNT (including the central hollow region), whose stiffness tensor was previously homogenized by using the strain energy of the CNT, while the outermost phase (N-th phase) represents the matrix; all phases in between (from 2 to $N-1$) correspond to different layers modeling the interphase; see Figure 6. The matrix was considered to be an isotropic material with an elastic modulus of 1 GPa and a Poisson's ratio of 0.35, simulating a typical engineering polymer [Fink 2010; Mittal 2011]. In order to model different CNT volume fractions in a composite, the thickness of the outermost phase was varied. The first phase (CNT) starts at $r = 0$ and ends at $r = R + \frac{1}{2}t$, which represents the interface with the first layer of interphase. The last layer

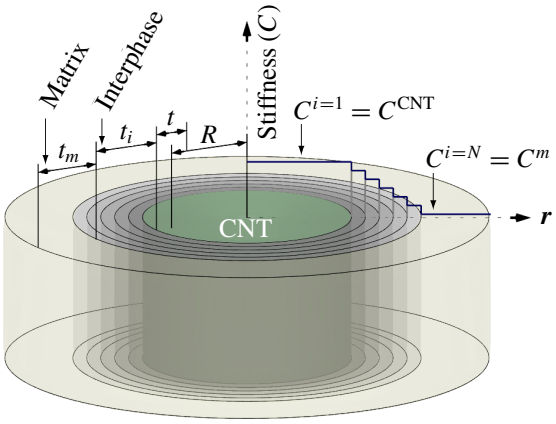

Figure 6. Schematic of the composite cylinder model.

of the interphase $(N-1)$ ends at $r = r_{N-1} = R + \frac{1}{2}t + t_i$, where t_i is the i-th interphase thickness. The thickness of the CNT/matrix interphase was set equal to the SWCNT wall thickness ($t_i = t$) as suggested in [Hernández-Pérez and Avilés 2010]. Finally, the matrix ends at $r = r_N = R + \frac{1}{2}t + t_i + t_m$, where t_m is the matrix thickness.

Since all phases have the same length and axial direction, the volume fraction of the CNT/polymer composite (v_f) is calculated as

$$v_f = \left[\frac{R + \frac{1}{2}t}{R + \frac{1}{2}t + t_i + t_m}\right]^2. \tag{6}$$

The maximum volume fraction available for each CNT ($v_{f\,\max}$) is obtained when $t_m = 0$, i.e.,

$$v_{f\,\max} = \left[\frac{R + \frac{1}{2}t}{R + \frac{1}{2}t + t_i}\right]^2. \tag{7}$$

The CCM was conducted for each armchair CNT chirality discussed in Section 2.2 — (3, 3) to (10, 10) — as well as for the two scenarios of damage generation depicted in Figure 5.

2.3.2. *Loading cases.* Four loading cases were used to obtain the five independent transversely isotropic elastic properties of CNT/polymer composites containing defective CNTs. These loading cases are similar to those depicted in Figure 4 for the CNTs, but for the continuous composites E_{11} and ν_{12} were extracted directly from the axial strain loading case. The four loading cases used to compute the elastic properties of the axially oriented CNT/polymer composites by the CCM are illustrated in Figure 7.

Figure 7a shows the loading case used to calculate the axial elastic modulus (E_{11}) and transverse Poisson's ratio (ν_{12}) of the composites. An axial displacement is applied and radial contraction is allowed. Detailed information about the system of equations for the boundary conditions, continuity, and displacement fields is included in Section A.1 of the Appendix. Once the system of equations is solved, the axial elastic modulus, E_{11}, is obtained as

$$E_{11} = \bar{\sigma}_{11}/\bar{\epsilon}_{11}, \tag{8}$$

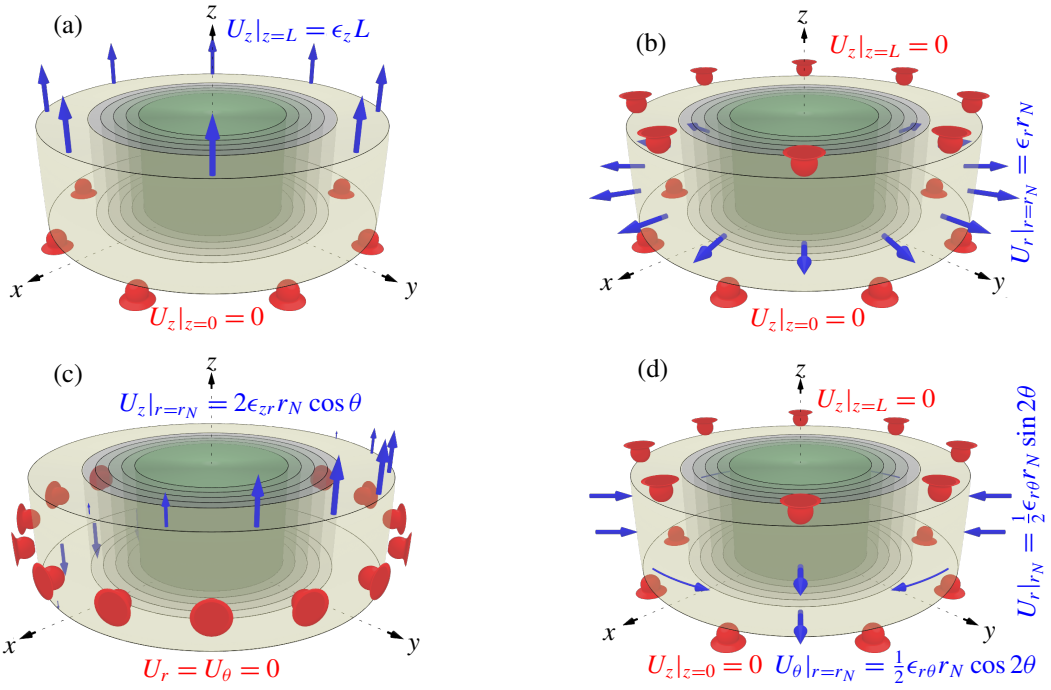

Figure 7. Loading cases used in the composite cylinder method: a, axial strain; b, in-plane bulk strain; c, transverse shear strain; and d, in-plane shear strain.

where $\bar{\sigma}_{11}$ and $\bar{\epsilon}_{11}$ are volumetric averages of the axial stress (σ_{11}) and axial strain (ϵ_{11}). The Poisson's ratio is calculated as

$$\nu_{12} = -\bar{\epsilon}_{22}/\bar{\epsilon}_{11}, \tag{9}$$

where $\bar{\epsilon}_{22}$ is the volumetric averaged radial strain which is equal to the radial strain at the outer surface ($r = r_N$).

Figure 7b shows the loading case used to calculate the in-plane bulk modulus of the composite (K_{23}). The axial displacements are restricted at $z = 0$ and $z = L$ and a radial displacement is applied at $r = r_N$. The system of equations stated in Section A.2 of the Appendix is solved and the in-plane bulk modulus is obtained as

$$K_{23} = \bar{\sigma}_{22}/2\bar{\epsilon}_{22}, \tag{10}$$

where $\bar{\sigma}_{22}$ and $\bar{\epsilon}_{22}$ are volumetric averages of the radial stress (σ_{22}) and the radial strain (ϵ_{22}).

Figure 7c shows the loading case used to calculate the transverse shear modulus of the composite (μ_{12}). For this loading case, all radial and tangential displacements are restricted and a transverse shear strain is produced by applying an axial displacement at $r = r_N$ as a function of θ. Analytical expressions for modeling such displacement conditions are presented in Section A.3 of the Appendix. The transverse shear modulus is then obtained from statement of equivalent surface tractions between the composite cylinder assemblage and the effective homogeneous cylinder, i.e.,

$$\mu_{12}^N \epsilon_{12}^N|_{r=r_N} = \mu_{12}\epsilon_{12}|_{r=r_N}, \tag{11}$$

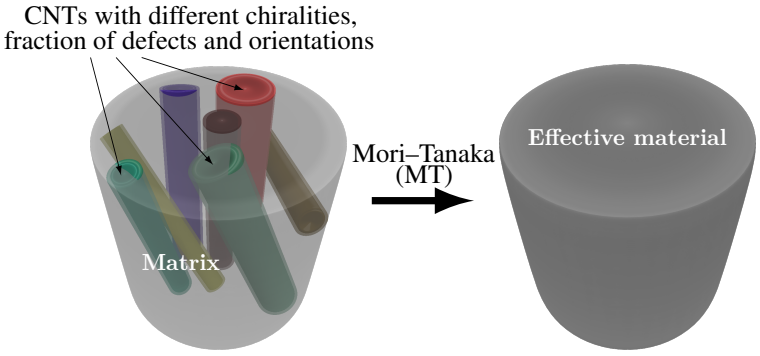

Figure 8. Mori–Tanaka approach for CNT/polymer composites.

where μ_{12}^N and ϵ_{12}^N are the transverse shear modulus and strain of the N-th phase, and μ_{12} and ϵ_{12} are the transverse shear modulus and strain of the effective homogeneous cylinder.

Figure 7c shows the loading case used to calculate the in-plane shear modulus of the composite (μ_{23}). Following Seidel and Lagoudas' methodology [2006], the generalized self-consistent composite cylinder method is employed to obtain the in-plane shear modulus (μ_{23}). This method is different from the conventional CCM because μ_{23} is not calculated by using its definition once the strains are obtained, but μ_{23} is explicitly included as an additional variable in the system of equations; see Section A.4 of the Appendix.

2.4. ***Mori–Tanaka approach for CNT/polymer composites.*** The Mori-Tanaka (MT) method allows for the prediction of elastic properties of a composite material constituted by different phases, each of them with its own geometry and material properties [Mori and Tanaka 1973]. The MT method is used here to predict the stiffness tensor of a CNT/polymer composite containing CNTs with different chiralities, fractions of broken bonds, and orientations; see Figure 8. The elastic properties of each phase are obtained from the CCM calculations in order to include the interphase.

In the MT method, the stiffness tensor (C) of the composite material is obtained as [Mori and Tanaka 1973]

$$C = \left(v_m C_m A_m + \sum_{i=1}^{N} v_i C_i A_i \right) \cdot \left(v_m I + \sum_{i=1}^{N} v_i A_i \right)^{-1}, \tag{12}$$

where I is the identity tensor (in Voigt's notation), C_m is the stiffness tensor of the polymer matrix, C_i is the stiffness tensor of the i-th phase, v_m is the volume fraction of the matrix phase, v_i is the volume fraction of the i-th phase, N is the total number of phases, A_i is the dilute strain concentration tensor for the i-th phase, transferring the strain applied on the composite to the coordinate system of each embedded phase. There are different ways to obtain A_i, one of those is by using an Eshelby [1957; 1959] tensor. Herein, the tensors are solved as matrices using Voigt's notation. Using an Eshelby tensor and an energetic equivalence between an inclusion with residual stresses and the phase to be modeled, the dilute strain concentration tensor for the i-th phase is [Lagoudas et al. 1991]

$$A_i = [I + S_i C_m^{-1} (C_i - C_m)]^{-1}, \tag{13}$$

where S_i is the Eshelby tensor for the i-th phase assumed as a cylindrical inclusion.

In order to compute the stiffness tensor of composites reinforced with randomly oriented CNTs, a rotational transformation is applied to both the strain concentration tensor and the stiffness matrix of each phase. The rotational transformations applied are of the form

$$X^* = \tilde{Q} \cdot X \cdot \tilde{Q}^T, \tag{14}$$

where X is the tensor (Voigt's notation) to be rotated and $\tilde{Q}$ is a 6×6 matrix constructed from $Q = Q(\theta, \phi)$, which is a 3×3 rotation matrix defined by

$$Q(\theta, \phi) = \begin{pmatrix} \cos(\theta)\sin(\phi) & \sin(\theta)\sin(\phi) & \cos(\phi) \\ -\sin(\theta) & \cos(\theta) & 0 \\ -\cos(\theta)\cos(\phi) & -\sin(\theta)\cos(\phi) & \sin(\phi) \end{pmatrix}, \tag{15}$$

where θ and ϕ are the two angular spherical coordinates.

In order to model a random orientation of CNTs, a volumetric average is applied to (12) to obtain

$$C = (v_m C_m A_m + O_1) \cdot (v_m I + O_2)^{-1}, \tag{16}$$

where

$$O_1 = \sum_{i=1}^{N} \frac{v_i}{4\pi} \int_0^{2\pi} \int_0^{\pi} \tilde{Q} \cdot C_i \cdot \tilde{Q}^T \cdot \tilde{Q} \cdot A_i \cdot \tilde{Q}^T \sin\phi \, \partial\phi \, \partial\theta, \tag{17a}$$

$$O_2 = \sum_{i=1}^{N} \frac{v_i}{4\pi} \int_0^{2\pi} \int_0^{\pi} \tilde{Q} \cdot A_i \cdot \tilde{Q}^T \sin\phi \, \partial\phi \, \partial\theta. \tag{17b}$$

3. Results

3.1. *Transversely isotropic elastic properties of pristine and defective CNTs.*

3.1.1. *Pristine CNTs.* The five transversely isotropic elastic properties of CNTs predicted by atomistic FEA are shown in Figure 9. The axial elastic modulus (E_{11}^{CNT}) presents a linearly decreasing trend with increased CNT's radius. The radial elastic modulus (E_{22}^{CNT}; see Figure 9, left) and both shear moduli (μ_{12}^{CNT} and μ_{23}^{CNT}; see Figure 9, right) present also a slightly decreasing trend with increased CNT radius. This trend is produced as a consequence of the larger proportion of inner hollow area inside the CNT as the radius increases, whereas all the considered carbon atoms are located at the outer ring. The proportion between the hollow center and the outer ring is larger for CNTs with larger radii. The results of E_{11}^{CNT} are within the range of previous predictions [Li and Chou 2003b; Lu 1997; Chang and Gao 2003; Xiao et al. 2005; Ávila and Lacerda 2008] and experiments [Treacy et al. 1996; Yu et al. 2000] by other authors, and also agrees with a previous work [Domínguez-Rodríguez et al. 2014] where CNTs were homogenized as hollow tubes. Those predictions of E_{11}^{CNT} are around 1 TPa and in the range of our calculations for small radius CNTs, i.e., (3, 3) and (4, 4) CNTs, where the central hollow area is much smaller than the tubular one. Using molecular mechanics, Shen and Li [2004] modeled the elastic properties of CNTs homogenized as solid cylinders and found a similar decreasing trend of the axial elastic modulus as a function of the CNT radius. However, some other authors have predicted higher values of E_{11}^{CNT} ($1 - 7$ TPa) [Tserpes and Papanikos 2005; Yakobson et al. 1996; Pantano et al. 2004] as a consequence of the CNT transverse area, which was assumed smaller [Ávila and Lacerda 2008]. The

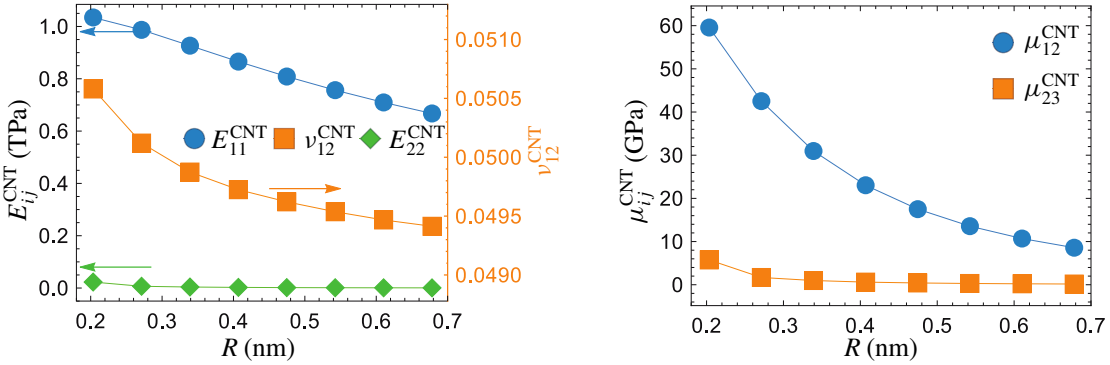

Figure 9. Elastic properties of SWCNTs as a function of their radius: left, axial and radial elastic moduli and transverse Poisson's ratio; right, transverse and in-plane shear moduli.

Poisson's ratio also presented a slight decreasing trend as a function of the CNT radius, but the difference in ν_{12} (Figure 9, left) for the different CNTs investigated is less than 2%. The radial elastic modulus of CNTs (E_{22}^{CNT}) is two orders of magnitude smaller than E_{11}^{CNT} (see Figure 9, left) which has similarly been observed experimentally [Palaci et al. 2005]. A possible explanation can be based on the loading paths. During axial strain, the deformation requires the stretching of the C-C bonds, whereas for a radial strain, most of the deformation is due to the more compliant bending of the C-C bonds.

3.1.2. *Damaged CNTs.* When the C-C bonds break, there is a probability for the CNT to become discontinuous, which renders singularities in the FEA displacement matrix. This probability is different if the bonds are removed randomly or by using a clustering pattern. In order to investigate the maximum fraction of broken bonds feasible in the CNT models, the bonds were removed following random and clustering damage processes. The process was repeated 200 times for a (3, 3) CNT and the continuity of the CNT structure was observed for each fraction of broken bonds. The fragmentation probability was defined as the number of fragmented CNTs divided by the total number of evaluated CNTs (200). According to Figure 10, this fragmentation probability resembles a sigmoid function of the fraction of broken bonds, especially for clustered damage. For random damage — Figure 10, left — the plotted interval (from 0 to 10%) only covers the first half of the sigmoid function. This phenomenon is markedly more pronounced for clustered damage (Figure 10, right), whose fragmentation probability is ~ 0.9 at a fraction of broken bonds of 8%, in comparison to ~ 0.25 for random damage at the same fraction of broken bonds. Fractions of defects higher than 8% render fragmentation probabilities for clustered damage close to 1, which is inappropriate for modeling purposes. Therefore, the highest fraction of broken bonds considered hereafter for clustered damage is 8%, whereas for random damage the maximum fraction of broken bonds was 10%.

The elastic properties of the defective CNTs were computed for the eight studied chiralities, varying the fraction of broken bonds. Figure 11 shows normalized plots of the axial elastic modulus for the studied SWCNTs with both random (Figure 11, left) or clustered (Figure 11, right) damage. E_{11}^{CNT} represents the axial elastic modulus of the defective CNT, while $E_{11}^{CNT^0}$ represents that of the pristine (defect-free) one. The axial elastic modulus of all the investigated SWCNTs decreases drastically as the fraction of broken bonds increases, which is in qualitative agreement with previous works [Sammalkorpi et al. 2004; Talukdar and Mitra 2010; Fefey et al. 2011; Yuan and Liew 2009]. This decrement is as

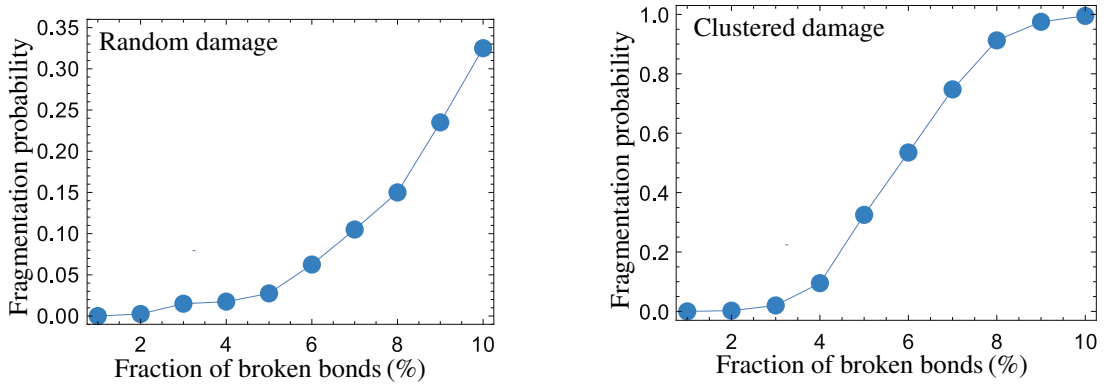

Figure 10. Probability of fragmentation as a function of the CNT fraction of broken bonds for a (3, 3) SWCNT: left, random damage; right, clustered damage.

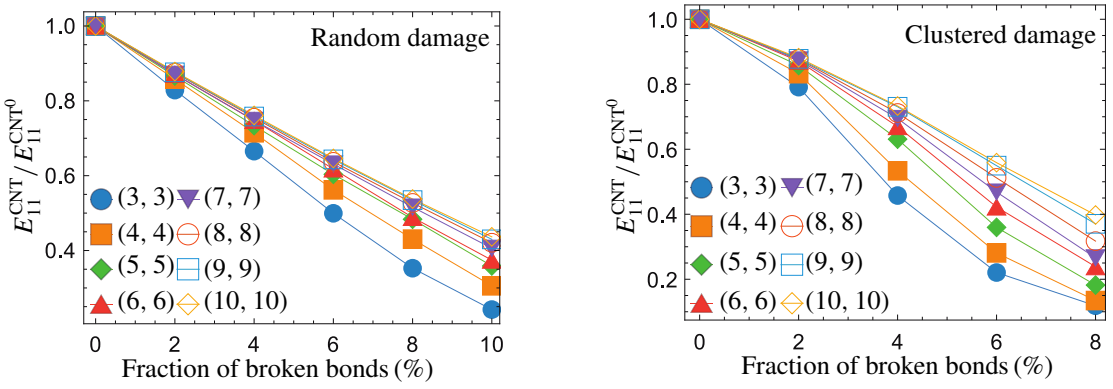

Figure 11. Normalized axial elastic modulus of defective CNTs as a function of the damage fraction: left, random damage; right, clustered damage.

high as $\sim 80\%$ for a 10% fraction of randomly distributed broken bonds (Figure 11, left) and as high as $\sim 85\%$ for a fraction of 8% clustered broken bonds (Figure 11, right). SWCNTs with smaller radii are more affected by structural defects because their unit cells have less C-C bonds (18 bonds for a unit cell of a (3, 3) SWCNT) than those of larger radii (60 bonds for a unit cell of a (10, 10) SWCNT).

The transverse Poisson's ratio of SWCNTs presents an increasing trend with an increased fraction of broken bonds (Figure 12). The value of ν_{12}^{CNT} increases six times with respect to the value of pristine CNTs for a fraction of 10% randomly distributed broken bonds (Figure 12, left). For clustered damage (Figure 12, right) the effect is more severe, reaching seven times the pristine value for an 8% fraction of broken bonds. This means that a defective CNT is significantly more compliant in the radial direction by Poisson's contraction than a pristine one. As for the case of the normalized axial elastic modulus, the difference from the pristine property is more prominent for defective SWCNTs with small radii, whose unit cells have less C-C bonds.

Similar to the case of E_{11}^{CNT}, the normalized radial elastic modulus (E_{22}^{CNT}) of defective CNTs (Figure 13) shows a linear decreasing trend with an increasing fraction of broken bonds. However, the reduction in E_{22}^{CNT} with the fraction of broken bonds is less severe than for E_{11}^{CNT} for both kinds of damage considered

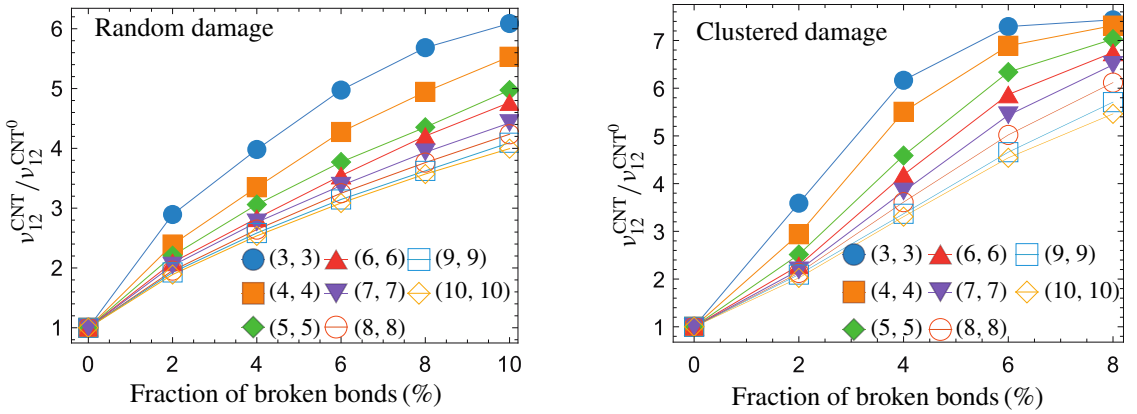

Figure 12. Normalized transverse Poisson's ratio of defective CNTs as a function of the damage fraction: left, random damage; right, clustered damage.

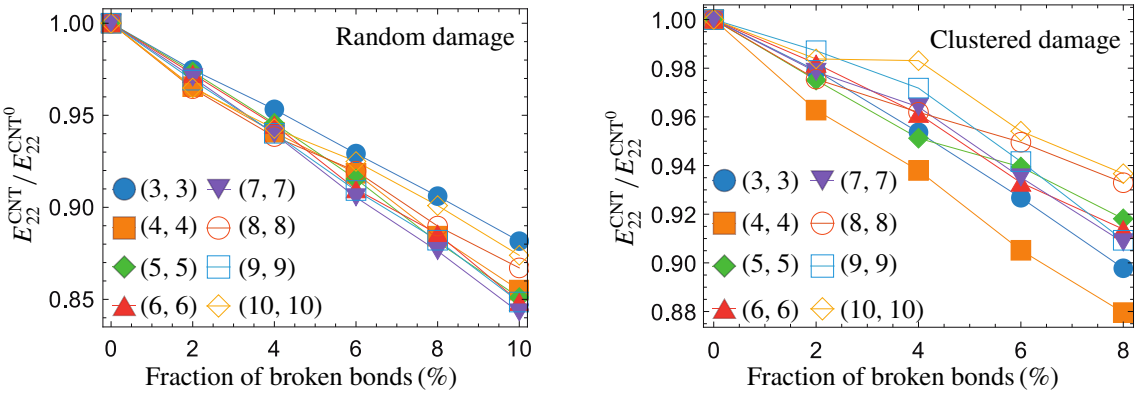

Figure 13. Normalized radial elastic modulus of defective CNTs as a function of the damage fraction: left, random damage; right, clustered damage.

herein. This is a consequence of the loading paths, because the probability of breaking a loading path is higher in the axial direction than in the radial one. The maximum reduction in E_{22}^{CNT} is $\sim 15\%$ for the case of random damage (Figure 13, left) and $\sim 12\%$ for the case of clustering damage (Figure 13, right).

The transverse shear modulus (μ_{12}^{CNT}, Figure 14) and the in-plane shear modulus (μ_{23}^{CNT}, Figure 15) of defective CNTs also present a decreasing trend as a function of the fraction of broken bonds. The decrease in the transverse shear modulus, Figure 14, is $\sim 14\%$ for a fraction of broken bonds of 10% for random damage, and $\sim 10\%$ for a fraction of broken bonds of 8% for clustered damage. The maximum reduction in the in-plane shear modulus, Figure 15, is $\sim 15\%$ for random damage and $\sim 12\%$ for clustered damage. As seen from these figures, the influence of the fraction of broken bonds on the transverse and in-plane elastic properties is smaller than on the axial elastic modulus, as a consequence of the loading paths.

3.2. Influence of CNT fraction of broken bonds on the transversely isotropic elastic properties of axially oriented CNT/polymer composites. The transversely isotropic elastic properties of CNT/polymer composites containing axially oriented (aligned) CNTs were first obtained by the CCM for each damaged SWCNT investigated. The computations were also conducted using the MT method to simulate

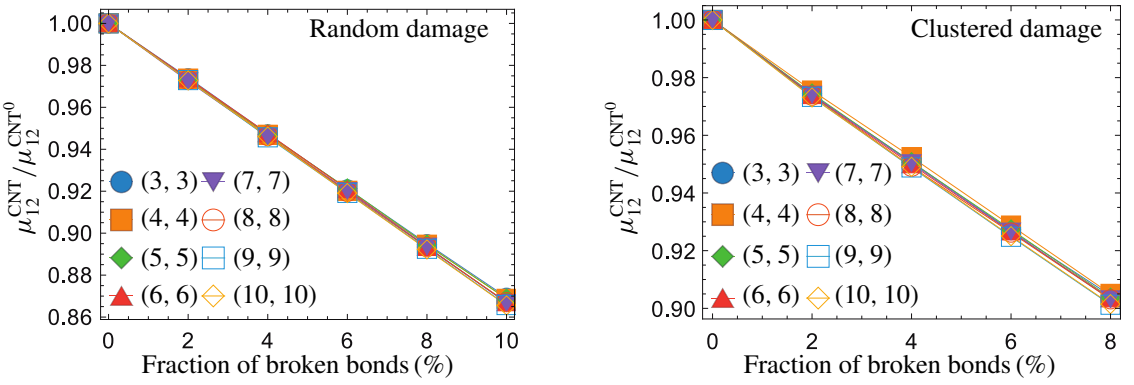

Figure 14. Normalized transverse shear modulus of defective CNTs as a function of the damage fraction: left, random damage; right, clustered damage.

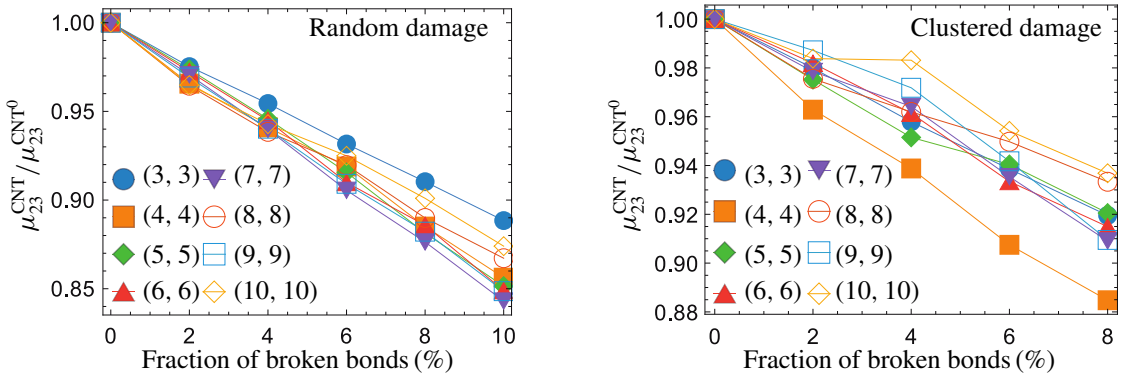

Figure 15. Normalized in-plane shear modulus of defective CNTs as a function of the damage fraction: left, random damage; right, clustered damage.

a CNT/polymer composite containing a full variety of axially oriented SWCNTs, including the eight studied chiralities and all different fractions of broken bonds, as could be expected in an experimental situation. For the MT method, the volume fraction of each chirality and fraction of broken bonds was calculated by sampling a random number from 0 to 1 following a uniform distribution of probability, and then weighted by the summation of volume fractions.

The influence of the fraction of broken bonds on the elastic properties of aligned CNT/polymer composites with a fixed CNT volume fraction of 1% was investigated for both random and clustered damage. The elastic properties reported in Figures 16–18 are normalized by the elastic property of the composite containing pristine CNTs (without defects), which are labeled with a superscript "0". The normalized axial elastic modulus of the composite (E_{11}/E_{11}^0) is plotted in Figure 16. E_{11} decreases linearly with increased fraction of broken bonds, regardless of the CNT size/chirality. The composite containing (3, 3) SWCNTs shows a more pronounced influence of the fraction of broken bonds as a consequence of the higher elastic properties of the (3, 3) CNT. For a fraction of SWCNT defects of 8%, the composite presents a knockdown in E_{11} of $\sim 60\%$ for random damage (Figure 16, left) and $\sim 80\%$ for clustered damage (Figure 16, right).

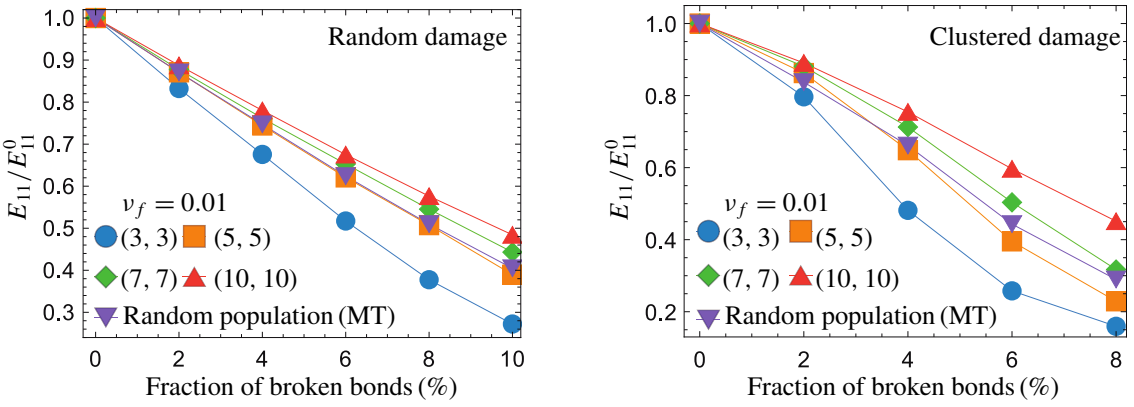

Figure 16. Normalized transverse axial elastic modulus of CNT/polymer composites as a function of CNT fraction of broken bonds for composites containing axially oriented CNTs: left, random damage; right, clustered damage.

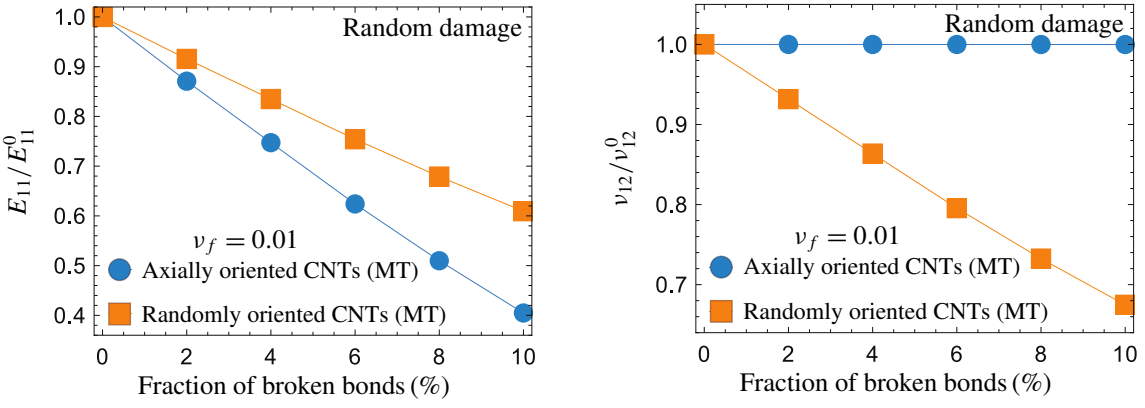

Figure 17. Normalized elastic properties of CNT/polymer composites as a function of the fraction of broken bonds for composites containing axially and randomly oriented CNTs: left, axial elastic modulus; right, transverse shear modulus.

The normalized transverse Poisson's ratio (ν_{12}/ν_{12}^0) of the composite as a function of the fraction of broken bonds is shown in Figure 18 for composites with axially oriented CNTs and a volume fraction of 1%. The value of ν_{12} increases as the fraction of CNT broken bonds increases due to lost of radial rigidity caused by the breakage of C-C bonds. This increase in ν_{12} is more pronounced for composites containing SWCNTs with smaller radii and clustered damage. However, the increments of ν_{12} are less than 5% for the maximum clustered fraction broken bonds investigated herein (8%).

The radial elastic modulus (E_{22}), the in-plane shear modulus (μ_{23}), and the transverse shear modulus (μ_{12}) were not significantly affected by the fraction of broken bonds for composites with axially oriented CNTs and therefore are not shown. This is because the in-plane and transverse elastic properties of unidirectional composites are matrix dominated, which also applies for the case of aligned CNTs.

3.3. ***Elastic properties of randomly oriented CNT/polymer composites.*** The elastic properties of CNT/polymer composites were also computed for SWCNTs with a variety of random orientations considering

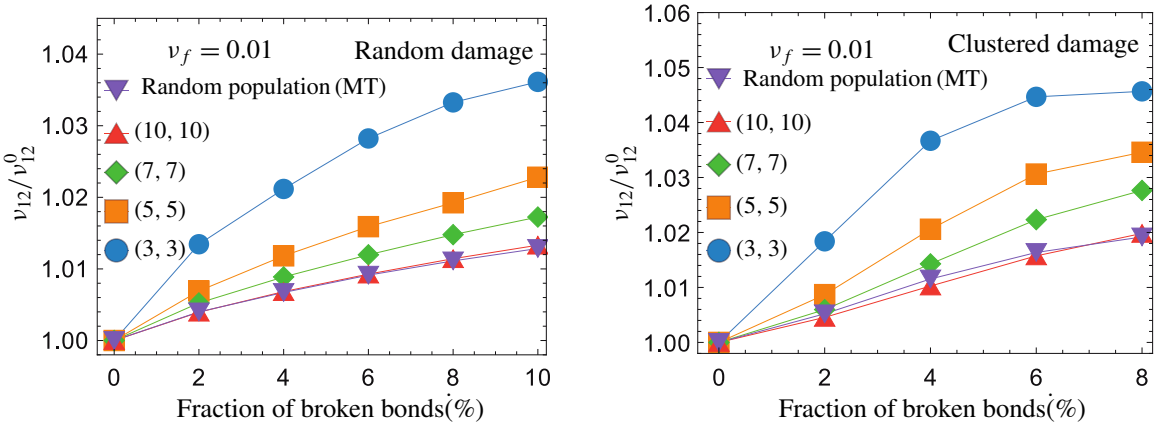

Figure 18. Normalized transverse Poisson's ratio of CNT/polymer composites as a function of CNT fraction of broken bonds for composites containing axially oriented CNTs: left, random damage; right, clustered damage.

pristine and defective CNTs and a fixed CNT volume fraction of 1% ($v_f = 0.01$). The MT formulation and (16) are used to average the elastic properties of CNT/polymer composites for all angle orientations, chirality, and fraction of defects. The normalized axial elastic modulus of CNT/polymer composites (E_{11}/E_{11}^0) as a function of the fraction of broken bonds is shown in Figure 17, left, for composites with axially and randomly oriented CNTs. Both random and clustered damage presented similar results; therefore, only plots for random damage are shown. The decreasing rate of E_{11}/E_{11}^0 for composites with axially oriented SWCNTs is larger, which is a consequence of the higher SWCNT influence on the composite elastic properties when the CNTs are axially oriented in the (unidirectional) composite.

The transverse shear modulus (μ_{12}), in-plane shear modulus (μ_{23}), and radial elastic modulus (E_{22}) are dominated by the matrix properties. As such, the contribution of the SWCNT (defective or not) is negligible when the SWCNTs are axially oriented, as shown in Figure 17, right, for the normalized transverse shear modulus. The in-plane shear modulus (μ_{23}) and the radial elastic modulus (E_{22}) as functions of the fraction of broken bonds present a similar trend to μ_{12} and therefore are not plotted. When the SWCNTs are randomly oriented, some of them reinforce the transverse direction and some others the axial one. Therefore, for a random orientation of SWCNTs, μ_{12}, μ_{23}, and E_{22} are significantly affected.

4. Conclusions

A multiscale hierarchical (sequential) approach was carried out to predict the influence of CNT structural defects on the elastic properties of CNT/polymer composites. As the initial step, the elastic properties of armchair SWCNTs were modeled using atomistic finite element analysis. Structural defects were generated in the SWCNTs by removing carbon-carbon bonds. SWCNT damage was produced progressively by randomly selecting the bonds to eliminate and also as a clustered (coalesced) damage by removing only bonds that are adjacent to the already eliminated bonds. The next step was the computation of the elastic properties of CNT/polymer composites, which was performed through the composite cylinder and Mori–Tanaka methods. The composite cylinder method was used to model the elastic properties of a composite

material containing axially oriented (aligned) CNTs surrounded by an interphase and matrix. The Mori–Tanaka method was used to model composite materials containing axially and randomly oriented CNTs with a random combination of chiralities and fractions of broken bonds. Regarding the elastic properties of CNTs, the knockdown in the axial elastic modulus of CNTs is on the order of $\sim 60\%$ with an 8% fraction of randomly broken bonds, whereas the knockdown with an 8% fraction of clustered broken bonds is $\sim 80\%$. The transverse Poisson's ratio of CNTs increases ~ 7 times with an 8% fraction of randomly or clustered broken bonds with respect to its pristine value. The radial elastic modulus, transverse shear modulus, and in-plane shear modulus of CNTs present a knockdown of about 10% for an 8% fraction of broken bonds. Regarding the elastic properties of CNT/polymer composites reinforced with axially oriented CNTs, the axial elastic modulus and the transverse Poisson's ratio are the elastic properties most influenced by the SWCNTs, and as such those properties are more affected by CNT defects. The knockdown in the axial elastic modulus for CNT/polymer composites containing a 1% volume fraction of randomly oriented CNTs with a fraction of broken bonds of 8% is on the order of $\sim 50\%$. The radial elastic modulus, the axial shear and the in-plane shear moduli of the CNT/polymer composites are only influenced by structural defects when the CNTs are randomly oriented. The knockdown in those properties are on the order of $\sim 30\%$ with a 1% CNT volume fraction and 8% fraction of defects. For randomly oriented CNTs, the five studied elastic properties are strongly influenced by the fraction of broken bonds. In comparison to random damage, clustered damage showed a larger influence of defects on the axial elastic modulus and transverse Poisson's ratio of CNTs (especially for those with smaller radius) and therefore, their polymer composites.

Appendix: Loading cases in the composite cylinder method

This appendix provides explicit equations concerning displacement fields, boundary conditions and continuity equations for the four loading cases used in the composite cylinder method.

A.1. ***Axial elastic modulus and transverse Poisson's ratio.*** For the axial elastic modulus (E_{11}), the radial (u_r^i), axial (u_z^i), and angular (u_θ^i) displacements of each phase (i) are defined in the interval $r_{i-1} \leq r \leq r_i$ as

$$u_r^i = B_1^i r + B_2^i/r, \quad u_\theta^i = 0, \quad u_z^i = \epsilon_z z, \tag{A.1}$$

where B_1^i and B_2^i are constants.

The outer surface of the composite at $r = r_N$ is free from radial stress, i.e.,

$$\sigma_{rr}^N|_{r=r_N} = 0. \tag{A.2}$$

In order to avoid a mathematical singularity, $B_2^{(1)}$ is set to 0 for the first layer.

The continuity equations for stresses and displacements of each layer are

$$u_r^i|_{r=r_i} = u_r^{i+1}|_{r=r_i}, \tag{A.3a}$$

$$\sigma_{rr}^i|_{r=r_i} = \sigma_{rr}^{i+1}|_{r=r_i}. \tag{A.3b}$$

A.2. ***In-plane bulk modulus.*** The in-plane bulk modulus (K_{23}) is calculated by using displacement equations for the interval $r_{i-1} \leq r \leq r_i$, which are similar to those of (A.1) except for the condition in u_z,

i.e.,

$$u_r^i = D_1^i r + D_2^i / r, \quad u_\theta^i = 0, \quad u_z^i = 0, \tag{A.4}$$

where D_1^i and D_2^i are constants.

The boundary conditions state that maximum radial displacement occurs at the outer surface ($r = r_N$), i.e.,

$$u_r^N|_{r=r_N} = \epsilon_r r_N. \tag{A.5}$$

$D_2^{(1)}$ is again set to 0 to avoid singularities.

The continuity conditions for stresses and displacements are those stated in (A.3).

A.3. ***Transverse shear modulus.*** The transverse shear modulus is calculated by applying an axial displacement field as function of θ for the interval $r_{i-1} \le r \le r_i$:

$$u_r^i = 0, \quad u_\theta^i = 0, \quad u_z^i = (F_1^i r + F_2^i / r)\cos\theta. \tag{A.6}$$

This displacement field produces a pure transverse shear strain ($\epsilon_{z\theta} \neq 0$, $\epsilon_{zz} = \epsilon_{rr} = \epsilon_{\theta\theta} = \epsilon_{r\theta} = 0$).

The boundary conditions require that the maximum radial deformation occurs at $r = r_N$ (see Figure 7c), i.e.,

$$u_z^N|_{r=r_N} = 2\epsilon_{z\theta} r_N \cos\theta, \tag{A.7}$$

where $F_2^{(1)}$ is set to 0 for the first layer.

The continuity equation for displacements is represented by (A.3a), while that for stresses is

$$\mu_i \left.\frac{\partial u_z^i}{\partial r}\right|_{r=r_i} = \mu_{i+1} \left.\frac{\partial u_z^{i+1}}{\partial r}\right|_{r=r_i}. \tag{A.8}$$

A.4. ***In-plane shear modulus.*** The displacement conditions used in the in-plane shear strain loading case are [Christensen and Lo 1979]

$$u_r^i = \left[H_1^i r + H_2^i r^3 \left(\frac{\nu_{zr}^i}{3 - 2\nu_{zr}^i} \right) - H_3^i \frac{1}{r^3} + 2H_4^i \frac{1}{r} \left(\frac{\nu_{zr}^i - 1}{2\nu_{zr}^i - 1} \right) \right] \sin(2\theta), \tag{A.9a}$$

$$u_\theta^i = \left(H_1^i r + H_2^i r^3 + H_3^i \frac{1}{r^3} + 2H_4^i \frac{1}{r} \right) \cos(2\theta), \tag{A.9b}$$

$$u_z^i = 0. \tag{A.9c}$$

Both $H_3^{(1)}$ and $H_4^{(1)}$ are set to 0 in order to avoid a mathematical singularity at the first layer.

The generalized self-consistent composite cylinder model includes an extra $(N + 1)$ layer of material which does not represent one of the N phases of the composite cylinder but the homogenized composite material. This layer explicitly includes the in-plane shear modulus of the composite material (μ_{23}^{eff}) instead of the shear modulus of a specific layer. The displacement fields for this layer are defined as [Seidel and

Lagoudas 2006]

$$u_r^{N+1} = \frac{r_{N+1}}{4\mu_{23}^{\text{eff}}}\left[\frac{2r}{r_{N+1}} + H_5\left(\frac{r_{N+1}}{r}\right)^3 + 4(1-\nu_{23}^{\text{eff}})H_6\frac{r_{N+1}}{r}\right]\sin(2\theta), \tag{A.10a}$$

$$u_\theta^{N+1} = \frac{-r_{N+1}}{4\mu_{23}^{\text{eff}}}\left[-\frac{2r}{r_{N+1}} + H_5\left(\frac{r_{N+1}}{r}\right)^3 - 2(1-2\nu_{23}^{\text{eff}})H_6\frac{r_{N+1}}{r}\right]\cos(2\theta), \tag{A.10b}$$

$$u_z^{N+1} = 0. \tag{A.10c}$$

The continuity equations for u_r, u_θ, σ_{rr}, and $\sigma_{r\theta}$ are similar to those stated in (A.3).

In order to achieve an energetic homogenization, the whole composite is considered an effective homogeneous solid cylinder whose displacements are

$$u_r^* = \frac{r_{N+1}}{4\mu_{23}^{\text{eff}}}\left(\frac{2r}{r_{N+1}}\right)\sin(2\theta), \tag{A.11a}$$

$$u_\theta^* = \frac{-r_{N+1}}{4\mu_{23}^{\text{eff}}}\left(-\frac{2r}{r_{N+1}}\right)\cos(2\theta), \tag{A.11b}$$

$$u_z^* = 0. \tag{A.11c}$$

The composite cylinder and the homogenized solid cylinder are energetically equated through the use of the Eshelby [1957; 1959] formula

$$\int_0^{2\pi}\left[\sigma_{rr}^{N+1}u_r^* + \sigma_{r\theta}^{N+1}u_\theta^* - (\sigma_{rr}^* u_r^{N+1} + \sigma_{r\theta}^* u_\theta^{N+1})\right]_{r=r_N}\mathrm{d}\theta = 0. \tag{A.12}$$

Then the system of equations from (A.9) to (A.12) is solved and μ_{23}^{eff} corresponds to the reported value for μ_{23}.

Acknowledgments

This work was supported by CONACYT project No. 220513 of Dr. Avilés. The bilateral collaboration between CICY and Virginia Tech was possible through the CONACYT-NSF award No. 121257 (CONACYT) and OISE-1019395 (NSF).

References

[Ahangari et al. 2013] M. G. Ahangari, A. Fereidoon, M. Jahanshahi, and M. Ganji, "Electronic and mechanical properties of single-walled carbon nanotubes interacting with epoxy: a DFT study", *Physica E* **48** (2013), 148–156.

[Araujo et al. 2012] P. T. Araujo, M. Terrones, and M. S. Dresselhaus, "Defects and impurities in graphene-like materials", *Mater. Today* **15**:3 (2012), 98–109.

[Ávila and Lacerda 2008] A. F. Ávila and G. S. R. Lacerda, "Molecular mechanics applied to single-walled carbon nanotubes", *Mat. Res.* **11** (09 2008), 325–333.

[Balog et al. 2010] R. Balog, B. Jorgensen, L. Nilsson, M. Andersen, E. Rienks, M. Bianchi, M. Fanetti, E. Laegsgaard, A. Baraldi, S. Lizzit, Z. Sljivancanin, F. Besenbacher, B. Hammer, T. G. Pedersen, P. Hofmann, and L. Hornekaer, "Bandgap opening in graphene induced by patterned hydrogen adsorption", *Nat. Mater.* **9**:4 (2010), 315–319.

[Banhart 1999] F. Banhart, "Irradiation effects in carbon nanostructures", *Rep. Progr. Phys.* **62**:8 (1999), 1181–1221.

[Banhart et al. 2011] F. Banhart, J. Kotakoski, and A. V. Krasheninnikov, "Structural defects in graphene", *ACS Nano* **5**:1 (2011), 26–41.

[Berber and Oshiyama 2006] S. Berber and A. Oshiyama, "Reconstruction of mono-vacancies in carbon nanotubes: atomic relaxation vs. spin polarization", *Physica B* **376–377** (2006), 272–275.

[Blake et al. 2007] P. Blake, E. W. Hill, A. H. C. Neto, K. S. Novoselov, D. Jiang, R. Yang, T. J. Booth, and A. K. Geim, "Making graphene visible", *Appl. Phys. Lett.* **91**:6 (2007), 063124.

[Blanc et al. 2002] X. Blanc, C. Le Bris, and P.-L. Lions, "From molecular models to continuum mechanics", *Arch. Ration. Mech. Anal.* **164**:4 (2002), 341–381.

[Burnett et al. 2012] T. L. Burnett, R. Yakimova, and O. Kazakova, "Identification of epitaxial graphene domains and adsorbed species in ambient conditions using quantified topography measurements", *J. Appl. Phys.* **112**:5 (2012), 054308.

[Caillerie et al. 2006] D. Caillerie, A. Mourad, and A. Raoult, "Discrete homogenization in graphene sheet modeling", *J. Elasticity* **84**:1 (2006), 33–68.

[Chang and Gao 2003] T. Chang and H. Gao, "Size-dependent elastic properties of a single-walled carbon nanotube via a molecular mechanics model", *J. Mech. Phys. Solids* **51**:6 (2003), 1059–1074.

[Christensen and Lo 1979] R. M. Christensen and K. H. Lo, "Solutions for effective shear properties in three phase sphere and cylinder models", *J. Mech. Phys. Solids* **27**:4 (1979), 315–330.

[Cornell et al. 1995] W. D. Cornell, P. Cieplak, C. I. Bayly, I. R. Gould, K. M. Merz, D. M. Ferguson, D. C. Spellmeyer, T. Fox, J. W. Caldwell, and P. A. Kollman, "A second generation force field for the simulation of proteins, nucleic acids, and organic molecules", *J. Am. Chem. Soc.* **117**:19 (1995), 5179–5197.

[De Volder et al. 2013] M. F. L. De Volder, S. H. Tawfick, R. H. Baughman, and A. J. Hart, "Carbon nanotubes: present and future commercial applications", *Science* **339** (2013), 535–539.

[Demczyk et al. 2002] B. G. Demczyk, Y. M. Wang, J. Cumings, M. Hetman, W. Han, A. Zettl, and R. O. Ritchie, "Direct mechanical measurement of the tensile strength and elastic modulus of multiwalled carbon nanotubes", *Mater. Sci. Eng. A* **334**:1–2 (2002), 173–178.

[Domínguez-Rodríguez et al. 2014] G. Domínguez-Rodríguez, A. Tapia, and F. Avilés, "An assessment of finite element analysis to predict the elastic modulus and Poisson's ratio of singlewall carbon nanotubes", *Comput. Mat. Sci.* **82** (2014), 257–263.

[Dow and Huyer 1989] J. O. Dow and S. A. Huyer, "Continuum models of space station structures", *J. Aerospace Eng.* **2**:4 (1989), 220–238.

[Eshelby 1957] J. D. Eshelby, "The determination of the elastic field of an ellipsoidal inclusion, and related problems", *Proc. Roy. Soc. London. Ser. A.* **241** (1957), 376–396.

[Eshelby 1959] J. D. Eshelby, "The elastic field outside an ellipsoidal inclusion", *Proc. Roy. Soc. London. Ser. A* **252** (1959), 561–569.

[Fefey et al. 2011] E. G. Fefey, R. Mohan, and A. Kelkar, "Computational study of the effect of carbon vacancy defects on the Young's modulus of (6, 6) single wall carbon nanotube", *Mater. Sci. Eng. B* **176**:9 (2011), 693–700.

[Ferrari and Basko 2013] A. C. Ferrari and D. M. Basko, "Raman spectroscopy as a versatile tool for studying the properties of graphene", *Nat. Nano.* **8**:4 (2013), 235–246.

[Fink 2010] J. K. Fink, *Handbook of engineering and speciality thermoplastics*, Scrivener, Salem, Massachusetts, 2010.

[Fonseca Guerra et al. 1998] C. Fonseca Guerra, J. G. Snijders, G. te Velde, and E. J. Baerends, "Towards an order-N DFT method", *Theor. Chem. Acc.* **99**:6 (1998), 391–403.

[Fukushima et al. 2006] T. Fukushima, A. Kosaka, Y. Yamamoto, T. Aimiya, S. Notazawa, T. Takigawa, T. Inabe, and T. Aida, "Dramatic effect of dispersed carbon nanotubes on the mechanical and electroconductive properties of polymers derived from ionic liquids", *Small* **2**:4 (2006), 554–560.

[Gallo et al. 2007] M. Gallo, A. Favila, and D. Glossman-Mitnik, "DFT studies of functionalized carbon nanotubes and fullerenes as nanovectors for drug delivery of antitubercular compounds", *Chem. Phys. Lett.* **447**:1–3 (2007), 105–109.

[Gao et al. 2008] L. Gao, W. Ren, F. Li, and H.-M. Cheng, "Total color difference for rapid and accurate identification of graphene", *ACS Nano* **2**:8 (2008), 1625–1633.

[Gates et al. 2005] T. S. Gates, G. M. Odegard, S. J. V. Frankland, and T. C. Clancy, "Computational materials: multi-scale modeling and simulation of nanostructured materials", *Compos. Sci. Tech.* **65**:15–16 (2005), 2416–2434.

[Giannopoulos et al. 2013] G. I. Giannopoulos, A. P. Tsiros, and S. K. Georgantzinos, "Prediction of elastic mechanical behavior and stability of single-walled carbon nanotubes using bar elements", *Mech. Adv. Mater. Struct.* **20**:9 (2013), 730–741.

[Haghbin and Khalili 2014] A. Haghbin and S. M. R. Khalili, "Effect of chiral angle on tensile behavior modeling of single-walled carbon nanotubes", *Mech. Adv. Mater. Struct.* **21**:6 (2014), 505–515.

[Hashin and Rosen 1964] Z. Hashin and B. W. Rosen, "The elastic moduli of fiber-reinforced materials", *J.Appl. Mech.* **31**:2 (1964), 223–232.

[Hernández-Pérez and Avilés 2010] A. Hernández-Pérez and F. Avilés, "Modeling the influence of interphase on the elastic properties of carbon nanotube composites", *Comput. Mat. Sci.* **47**:4 (2010), 926–933.

[Hine et al. 2009] N. D. M. Hine, P. D. Haynes, A. A. Mostofi, C.-K. Skylaris, and M. C. Payne, "Linear-scaling density-functional theory with tens of thousands of atoms: expanding the scope and scale of calculations with ONETEP", *Comput. Phys. Comm.* **180**:7 (2009), 1041–1053.

[Jorgensen and Severance 1990] W. L. Jorgensen and D. L. Severance, "Aromatic-aromatic interactions: free energy profiles for the benzene dimer in water, chloroform, and liquid benzene", *J. Am. Chem. Soc.* **112**:12 (1990), 4768–4774.

[Kalamkarov et al. 2006] A. L. Kalamkarov, A. V. Georgiades, S. K. Rokkam, V. P. Veedu, and M. N. Ghasemi-Nejhad, "Analytical and numerical techniques to predict carbon nanotubes properties", *Int. J. Solids Struct.* **43**:22–23 (2006), 6832–6854.

[Kim et al. 2009] K. S. Kim, Y. Zhao, H. Jang, S. Y. Lee, J. M. Kim, K. S. Kim, J.-H. Ahn, P. Kim, J.-Y. Choi, and B. H. Hong, "Large-scale pattern growth of graphene films for stretchable transparent electrodes", *Nature* **457**:7230 (2009), 706–710.

[Kohn 1995] W. Kohn, "Density functional theory for systems of very many atoms", *Int. J. Quantum Chem.* **56**:4 (1995), 229–232.

[Krasheninnikov and Banhart 2007] A. V. Krasheninnikov and F. Banhart, "Engineering of nanostructured carbon materials with electron or ion beams", *Nat. Mater.* **6**:10 (2007), 723–733.

[Lagoudas et al. 1991] D. C. Lagoudas, A. C. Gavazzi, and H. Nigam, "Elastoplastic behavior of metal matrix composites based on incremental plasticity and the Mori–Tanaka averaging scheme", *Comput. Mech.* **8**:3 (1991), 193–203.

[Li and Chou 2003a] C. Li and T.-W. Chou, "Elastic moduli of multi-walled carbon nanotubes and the effect of van der Waals forces", *Compos. Sci. Tech.* **63**:11 (2003), 1517–1524.

[Li and Chou 2003b] C. Li and T.-W. Chou, "A structural mechanics approach for the analysis of carbon nanotubes", *Int. J. Solids Struct.* **40**:10 (2003), 2487–2499.

[Lu 1997] J. P. Lu, "Elastic properties of carbon nanotubes and nanoropes", *Phys. Rev. Lett.* **79** (1997), 1297–1300.

[Lucchese et al. 2010] M. Lucchese, F. Stavale, E. M. Ferreira, C. Vilani, M. Moutinho, R. B. Capaz, C. Achete, and A. Jorio, "Quantifying ion-induced defects and Raman relaxation length in graphene", *Carbon* **48**:5 (2010), 1592–1597.

[Meyer 2000] C. Meyer, *Matrix analysis and applied linear algebra and solutions manual*, Society for Industrial and Applied Mathematics, Philadelphia, 2000.

[Mielke et al. 2004] S. L. Mielke, D. Troya, S. Zhang, J.-L. Li, S. Xiao, R. Car, R. S. Ruoff, G. C. Schatz, and T. Belytschko, "The role of vacancy defects and holes in the fracture of carbon nanotubes", *Chem. Phys. Lett.* **390**:4–6 (2004), 413–420.

[Mittal 2011] V. Mittal, *High performance polymers and engineering plastics*, Scrivener, Salem, Massachusetts, 2011.

[Monthioux and Charlier 2014] M. Monthioux and J.-C. Charlier, "Giving credit where credit is due: the Stone–(Thrower)–Wales designation revisited", *Carbon* **75** (2014), 1–4.

[Mori and Tanaka 1973] T. Mori and K. Tanaka, "Average stress in matrix and average elastic energy of materials with misfitting inclusions", *Acta Metall.* **21**:5 (1973), 571–574.

[Natsuki et al. 2004] T. Natsuki, K. Tantrakarn, and M. Endo, "Effects of carbon nanotube structures on mechanical properties", *Appl. Phys. A* **79**:1 (2004), 117–124.

[Ni et al. 2007] Z. H. Ni, H. M. Wang, J. Kasim, H. M. Fan, T. Yu, Y. H. Wu, Y. P. Feng, and Z. X. Shen, "Graphene thickness determination using reflection and contrast spectroscopy", *Nano Lett.* **7**:9 (2007), 2758–2763.

[Noor 1988] A. K. Noor, "Continuum modeling for repetitive lattice structures", *Appl. Mech. Rev.* **41**:7 (1988), 285–296.

[Noor et al. 1978] A. K. Noor, M. S. Anderson, and W. H. Greene, "Continuum models for beam- and platelike lattice structures", *AIAA Journal* **16**:12 (1978), 1219–1228.

[Novoselov et al. 2005] K. S. Novoselov, D. Jiang, F. Schedin, T. J. Booth, V. V. Khotkevich, S. V. Morozov, and A. K. Geim, "Two-dimensional atomic crystals", *Proc. Nat. Acad. Sci. USA* **102**:30 (2005), 10451–10453.

[Obraztsova et al. 2008] E. A. Obraztsova, A. V. Osadchy, E. D. Obraztsova, S. Lefrant, and I. V. Yaminsky, "Statistical analysis of atomic force microscopy and Raman spectroscopy data for estimation of graphene layer numbers", *Physica Status Solidi (B)* **245**:10 (2008), 2055–2059.

[Odegard et al. 2002] G. M. Odegard, T. S. Gates, L. M. Nicholson, and K. E. Wise, "Equivalent-continuum modeling of nano-structured materials", *Compos. Sci. Tech.* **62**:14 (2002), 1869–1880.

[Palaci et al. 2005] I. Palaci, S. Fedrigo, H. Brune, C. Klinke, M. Chen, and E. Riedo, "Radial elasticity of multiwalled carbon nanotubes", *Phys. Rev. Lett.* **94** (2005), 175502–1–175502–4.

[Pantano et al. 2004] A. Pantano, D. M. Parks, and M. C. Boyce, "Mechanics of deformation of single- and multi-wall carbon nanotubes", *J. Mech. Phys. Solids* **52**:4 (2004), 789–821.

[Prasomsri et al. 2010] T. Prasomsri, D. Shi, and D. E. Resasco, "Anchoring Pd nanoclusters onto pristine and functionalized single-wall carbon nanotubes: a combined DFT and experimental study", *Chem. Phys. Lett.* **497**:1–3 (2010), 103–107.

[Qu and Cherkaoui 2006] J. Qu and M. Cherkaoui, *Fundamentals of micromechanics of solids*, Wiley, Hoboken, New Jersey, 2006.

[Sakhaee-Pour 2009] A. Sakhaee-Pour, "Elastic properties of single-layered graphene sheet", *Solid State Comm.* **149**:1–2 (2009), 91–95.

[Sammalkorpi et al. 2004] M. Sammalkorpi, A. Krasheninnikov, A. Kuronen, K. Nordlund, and K. Kaski, "Mechanical properties of carbon nanotubes with vacancies and related defects", *Phys. Rev. B* **70** (2004), 245416.

[Seidel and Lagoudas 2006] G. D. Seidel and D. C. Lagoudas, "Micromechanical analysis of the effective elastic properties of carbon nanotube reinforced composites", *Mech. Mater.* **38**:8–10 (2006), 884–907.

[Sharma et al. 2012] K. Sharma, K. K. Saxena, and M. Shukla, "Effect of multiple Stone–Wales and vacancy defects on the mechanical behavior of carbon nanotubes using molecular dynamics", *Procedia Engineering* **38** (2012), 3373–3380.

[Shen and Li 2004] L. Shen and J. Li, "Transversely isotropic elastic properties of single-walled carbon nanotubes", *Phys. Rev. B* **69** (2004), 045414–1–045414–10.

[Shet et al. 2005] C. Shet, N. Chandra, and S. Namilae, "Defect-defect interaction in carbon nanotubes under mechanical loading", *Mech. Adv. Mater. Struct.* **12**:1 (2005), 55–65.

[Spitalsky et al. 2010] Z. Spitalsky, D. Tasis, K. Papagelis, and C. Galiotis, "Carbon nanotube-polymer composites: chemistry, processing, mechanical and electrical properties", *Prog. Polymer Sci.* **35**:3 (2010), 357–401.

[Srivastava et al. 2003] D. Srivastava, C. Wei, and K. Cho, "Nanomechanics of carbon nanotubes and composites", *Appl. Mech. Rev.* **56**:2 (2003), 215–230.

[Sun and Liebbe 1990] C. T. Sun and S. W. Liebbe, "Global-local approach to solving vibration of large truss structures", *AIAA Journal* **28**:2 (1990), 303–308.

[Sun et al. 1981] C. Sun, B. Kim, and J. Bogdanoff, "On the derivation of equivalent simple models for beam- and platelike structures in dynamic analysis", in *Structures, structural dynamics, and materials and co-located conferences*, American Institute of Aeronautics and Astronautics, 1981.

[Talukdar and Mitra 2010] K. Talukdar and A. K. Mitra, "Comparative MD simulation study on the mechanical properties of a zigzag single-walled carbon nanotube in the presence of Stone–Thrower–Wales defects", *Compos. Struct.* **92**:7 (2010), 1701–1705.

[Treacy et al. 1996] M. M. J. Treacy, T. W. Ebbesen, and J. M. Gibson, "Exceptionally high Young's modulus observed for individual carbon nanotubes", *Nature* **381**:6584 (1996), 678–680.

[Tserpes and Papanikos 2005] K. I. Tserpes and P. Papanikos, "Finite element modeling of single-walled carbon nanotubes", *Compos. B* **36**:5 (2005), 468–477.

[Tserpes and Papanikos 2007] K. I. Tserpes and P. Papanikos, "The effect of Stone–Wales defect on the tensile behavior and fracture of single-walled carbon nanotubes", *Compos. Struct.* **79**:4 (2007), 581–589.

[Usik 1994] L. Usik, "Equivalent continuum models of large platelike lattice structures", *Int. J. Solids Struct.* **31**:4 (1994), 457–467.

[Xiao et al. 2005] J. R. Xiao, B. A. Gama, and J. W. Gillespie Jr., "An analytical molecular structural mechanics model for the mechanical properties of carbon nanotubes", *Int. J. Solids Struct* **42**:11–12 (2005), 3075–3092.

[Yakobson et al. 1996] B. I. Yakobson, C. J. Brabec, and J. Bernholc, "Nanomechanics of carbon tubes: instabilities beyond linear response", *Phys. Rev. Lett.* **76** (1996), 2511–2514.

[Yu et al. 2000] M.-F. Yu, B. S. Files, S. Arepalli, and R. S. Ruoff, "Tensile loading of ropes of single wall carbon nanotubes and their mechanical properties", *Phys. Rev. Lett.* **84** (2000), 5552–5555.

[Yuan and Liew 2009] J. Yuan and K. Liew, "Effects of vacancy defect reconstruction on the elastic properties of carbon nanotubes", *Carbon* **47**:6 (2009), 1526–1533.

[Zandiatashbar et al. 2014] A. Zandiatashbar, G.-H. Lee, S. J. An, S. Lee, N. Mathew, M. Terrones, T. Hayashi, C. R. Picu, J. Hone, and N. Koratkar, "Effect of defects on the intrinsic strength and stiffness of graphene", *Nat. Comm.* **5** (2014), 1–8.

[Zhang et al. 2002] P. Zhang, Y. Huang, P. H. Geubelle, P. A. Klein, and K. C. Hwang, "The elastic modulus of single-wall carbon nanotubes: a continuum analysis incorporating interatomic potentials", *Int. J. Solids Struct.* **39**:13–14 (2002), 3893–3906.

Received 25 Apr 2016. Revised 23 Nov 2016. Accepted 28 Nov 2016.

GUSTAVO DOMÍNGUEZ-RODRÍGUEZ: gashdmi@gmail.com
Centro de Investigación Científica de Yucatán, Calle 43 No. 130, Colonia Chuburná de Hidalgo, 97200 Mérida,, Yucatan, Mexico

ADARSH CHAURASIA: adarsh.chaurasia@vt.edu
Department of Engineering Science and Mechanics, Virginia Polytechnic Institute and State University, 495 Ol d Turner Street, Norris Hall, Room 223, Blacksburg, VA 24061, United States

GARY SEIDEL: gary.seidel@vt.edu
Department of Aerospace and Ocean Engineering, Virginia Polytechnic Institute and State University, 228 Randolph Hall (0203), Blacksburg, VA 24061, United States

ALEJANDRO TAPIA: jorge.tapia@correo.uady.mx
Facultad de Ingeniería, Universidad Autónoma de Yucatán, Av. Industrias no Contaminantes por Periférico, Norte, Cordemex, 97310 Mérida,, Mexico

FRANCIS AVILÉS: faviles@cicy.mx
Centro de Investigación Científica de Yucatán, Calle 43 No. 130, Colonia Chuburná de Hidalgo, 97200 Mérida,, Mexico

JOURNAL OF MECHANICS OF MATERIALS AND STRUCTURES

msp.org/jomms

Founded by Charles R. Steele and Marie-Louise Steele

See msp.org/jomms for submission guidelines.

JoMMS (ISSN 1559-3959) at Mathematical Sciences Publishers, 798 Evans Hall #6840, c/o University of California, Berkeley, CA 94720-3840, is published in 10 issues a year. The subscription price for 2017 is US $615/year for the electronic version, and $775/year (+$60, if shipping outside the US) for print and electronic. Subscriptions, requests for back issues, and changes of address should be sent to MSP.

JoMMS peer-review and production is managed by EditFLOW® from Mathematical Sciences Publishers.

PUBLISHED BY

mathematical sciences publishers

nonprofit scientific publishing

http://msp.org/

Journal of Mechanics of Materials and Structures

Volume 12, No. 3 May 2017

1559-3959(2017)12:3;1-2